Manuscript prepared for Ann. Geophys.
with version 1.3 of the LaTeX class copernicus.cls.
Date: 20 November 2021

Terrestrial exospheric dayside H-density profile at 3-15 $R_{\rm e}$ from UVIS/HDAC and TWINS Lyman-α data combined

Jochen H. Zoennchen[1], Hyunju K. Connor[2], Jaewoong Jung[2], Uwe Nass[1], and Hans J. Fahr[1]

[1]Argelander Institut für Astronomie, Astrophysics Department, University of Bonn, Auf dem Huegel 71,
53121 Bonn, Germany

[2]Geophysical Institute, University of Alaska Fairbanks, Alaska, USA

Correspondence to: J. H. Zoennchen (zoenn@astro.uni-bonn.de)

Abstract.

Terrestrial ecliptic dayside observations of the exospheric Lyman-α column intensity between 3-15 Earth radii ($R_{\rm e}$) by UVIS/HDAC at CASSINI have been analysed to derive the neutral exospheric H-density profile at the Earth's ecliptic dayside in this radial range. The data were measured during CASSINIS's swing by manoeuvre at the Earth on 18 August 1999 and are published by (Werner et al., 2004). In this study the dayside HDAC Lyman-α observations published by (Werner et al., 2004) are compared to calculated Lyman-α intensities based on the 3D H-density model derived from TWINS Lyman-α observations between 2008-2010 (Zoennchen et al., 2015). It was found, that both Lyman-α profiles show a very similar radial dependence in particular between 3-8 $R_{\rm e}$. Between 3.0-5.5 $R_{\rm e}$ impact distance Lyman-α observations of both TWINS and UVIS/HDAC are existing at the ecliptic dayside. In this overlapping region the cross-calibration of the HDAC profile against the calculated TWINS profile was done, assuming, that the exosphere there was similar for both due to comparable space weather conditions. As result of the cross-calibration the conversion factor between counts/s and Rayleigh f_c=3.285 [counts/s/R] is determined for these HDAC observations. Using this factor the radial H-density profile for the Earths ecliptic dayside was derived from the UVIS/HDAC observations, which constrained the neutral H-density there at 10 $R_{\rm e}$ to a value of 35 cm^{-3}. Furthermore, a faster radial H-density decrease was found at distances above 8 $R_{\rm e}$ ($\approx r^{-3}$) compared to the lower distances 3-7 $R_{\rm e}$ ($\approx r^{-2.37}$). This increased loss of neutral H above 8 $R_{\rm e}$ might indicate a higher rate of H ionization in the vicinity of the magnetopause at 9-11 $R_{\rm e}$ (near sub solar point) and beyond, because of increasing charge exchange interactions of exospheric H atoms with solar wind ions outside the magnetosphere.

Keywords. Atmospheric composition and structure (airglow and aurora; pressure, density, and temperature) – meteorology and atmospheric dynamics (thermospheric dynamics)

1 Introduction

The Earth's exosphere is the outermost layer of our atmosphere that ranges from ≈500km altitude to beyond the Moons orbit (Baliukin et al. 2019). Atomic hydrogen atom (H) becomes a dominant species above an altitude of ≈1500km. The exosphere gains and loses hydrogen atoms as a result of the Sun - solar wind - magnetosphere - upper atmosphere interaction. Study of the exospheric density distribution and its response to dynamic space environments is key to understand the past, present, and future of the Earths atmosphere and to infer the evolution of other planetary atmospheres.

The typical geocorona emission, i.e., solar Lyman-α photons resonantly scattered by hydrogen atoms, has been a widely used dataset to derive a terrestrial exospheric neutral H-density. Several spacecraft missions like Thermosphere - Ionosphere - Mesosphere Energetics and Dynamics (TIMED; Kusnierkiewicz, 1997), Two Wide-Angle Imaging Neutral- Atom Spectrometer (TWINS; Goldstein & McComas, 2018), and Solar and Heliospheric Observatory (SOHO; Domingo et al., 1995) have observed the geocorona from various vantage points, covering an optically thick, near-Earth exosphere below ≈3 $R_{\rm e}$ geocentric distance (e.g., Qin & Waldrop, 2016; Qin et al., 2017; Waldrop et al., 2013) to an optically thin, far distant exosphere on top (e.g., Bailey & Gruntman, 2011; Cucho-Padin & Waldrop, 2019; Zoennchen et al., 2011, 2013). The exospheric density changes over various time scales such as solar cycle (Waldrop & Paxton, 2013; Zoennchen et al., 2015; Baliukin et al., 2019), solar rotation (Zoennchen et al., 2015), and geomagnetic storms (Bailey & Gruntmann, 2013; Cucho-Padin & Waldrop, 2019; Qin et al., 2017; Zoennchen et al., 2017). This implies active response of our exosphere to a dynamic space environment through physical processes like thermal expansion, photoionization, and neutral charge exchanges as suggested in the previous theoretical studies (Chamberlain, 1963; Bishop, 1985; Hodges, 1994; and references therein). Also the possible contribution of non-thermal hydrogen to the exosphere is discussed (e.g., Qin & Waldrop, 2016; Fahr et al., 2018).

Recently, exospheric neutral H-density at 10 $R_{\rm e}$ subsolar location becomes a particular interest due to two upcoming missions, the NASA Lunar Environment heliospheric X-ray Imager (LEXI; http://sites.bu.edu/lexi) and the joint ESA-China mission, Solar wind - Magnetosphere - Ionosphere Link Explorer (SMILE; Branduardi-Raymont et al., 2018) with expected launches in 2023 and 2024, respectively. Soft X-ray imagers on these spacecrafts will observe motion of the Earths magnetosheath and cusps in soft X-ray with a primary goal of understanding the magnetopause reconnection modes under various solar wind conditions. Soft X-ray is emitted due to interaction between the exospheric neutrals and the highly charged solar wind ions like O^{7+} and O^{8+} (Sibeck et al., 2018; Connor et al., 2021). Neutral density is a key parameter that controls the strength of soft X-ray sig-

nals. Denser hydrogen increases their interaction probability with solar wind ions and thus enhance soft X-ray signals, which is preferable for the LEXI and SMILE missions.

The dayside geocoronal observations above 8 $R_{\rm e}$ radial distance are very rare. For estimating an exospheric density at 10 $R_{\rm e}$ subsolar location, Connor & Carter (2019) and Fuselier et al. (2010; 2020) used alternative datasets: the soft X-ray observations from the X-ray Multi-Mirror Mission-Newton astrophysics mission (XMM; Jansen et al., 2001) and the Energetic Neutral Atom (ENA) observations from the Interstellar Boundary Explorer (IBEX; McComas et al., 2009), respectively. Their density estimates at 10 $R_{\rm e}$ show a large discrepancy, ranging from 4 cm^{-3} to 59 cm^{-3} with a lower limit from the IBEX observations and an upper limit from the XMM observations. However, these studies analyzed only a handful of events. Additionally, inherent difference of the soft X-ray and ENA datasets leads to different density extraction techniques, possibly contributing to the neutral density discrepancy. To understand a true nature of this outer dayside exosphere, more statistical and cumulative approaches with various datasets are needed.

We estimate a dayside exospheric density in a radial distance of 3-15 $R_{\rm e}$ using rare dayside geocorona observations obtained from the CASSINI UVIS/HDAC Lyman-α instrument on 18 August 1999. This paper is structured as follows. Section 2 introduces the CASSINI Lyman-α observations on 18 August 1999. Section 3 discusses the solar condition and interplanetary Lyman-α background during the observation period. Section 4 explains our density extraction approach. Section 5 estimates the conversion factor of the CASSINI UVIS/HDAC geocorona count rates to Rayleigh, and Section 6 derives the dayside exospheric density profiles from the converted geocoronal emission in Rayleigh. Finally, Section 7 discusses and concludes our results.

2 The UVIS/HDAC Lyman-α observations during CASSINIs swing by at the Earth

On its way to Saturn the CASSINI spacecraft performed a swing by manoeuvre at the Earth on 18 August 1999. The UVIS/HDAC Lyman-α instrument (FOV $\approx 3^{\circ}$) was switched on before and measured then continuosly Lyman-α intensities during the manoeuvre. When approaching the Earth the measured Lyman-α intensities were increasingly dominated by scattered Lyman-α emission from neutral H-atoms of the terrestrial exosphere. The intensity profile in [counts/s] (averaged over a 1 min interval) from UVIS/HDAC is a rare observation of the exospheric dayside Lyman-α emission near the Earth-Sun line up to 15 $R_{\rm e}$ geocentric distance. It is a nearly perfect scan within the ecliptic plane during $\approx$ 1.5 hours and therefore nearly free from latitudinal and temporal variations. The profile was published by (Werner et al., 2004) and is shown in Figure 2 of their paper. From each measurement they had subtracted 4500 [counts/s] as correction for their estimate of the interplanetary background intensity. For the geocentric distances 3-15 $R_{\rm e}$ this corrected profile can be

numerically approximated by the following fit function:

$$I_{corr}(r) = 282920.2 * (r + 2.0)^{-2.2} \ \ [counts/s] \quad (1)$$

with the geocentric distance r in R_e. In Figure 1 is shown, that the fitted radial intensity function from Equation (1) (red line) approximates the profile from (Werner et al., 2004) (black line) very well. Values from Equation (1) need to be re-added with 4500 [counts/s] in order to retrieve the uncorrected intensities originally measured by UVIS/HDAC:

$$I(r) = I_{corr}(r) + 4500 \ \ [counts/s] \quad (2)$$

The observational geometry (spacecraft position and viewing direction of UVIS/HDAC) during the swing by was also adopted from (Werner et al., 2004): On the Earth dayside CASSINI moved within the ecliptic plane towards Earth. CASSINI's dayside trajectory as shown in (Werner et al., 2004 - see Figure 1 there) is nearly linear within 3-15 R_e. It can be numerically approximated as radial function of the GSE longitude:

$$\phi_{GSE}(r) = 6.7 + 80.14/r \ \ [^\circ] \quad (3)$$

with the geocentric distance r in R_e. Following (Werner et al., 2004) in this trajectory segment the line of sight (LOS) of UVIS/HDAC pointed towards the positive GSE Y-axis away from Earth. More UVIS/HDAC instrumental facts can be found in the "UVIS User's Guide" provided by NASA PDS-Website (see: https://pds-atmospheres.nmsu.edu/data_and_services/atmospheres_data/Cassini/inst-uvis.html)

3 Solar conditions and the interplanetary Lyman-α background

The total solar Lyman-α flux and the solar $F_{10,7cm}$-radio flux are important indicators of the solar activity. The solar Lyman-α flux can vary from 3.5 (solar minimum) to 6.5 (solar maximum) $\cdot 10^{11}$ [photons/cm^2/s]. The solar $F_{10,7cm}$-radio flux can vary from below 50 (solar minimum) to above 300 (solar maximum). On the swing by date 18 August 1999 the value of the total solar Lyman-α flux was 4.52 - a bit higher than the value of $\approx$ 3.5 during the TWINS LAD-observations in 2008 and 2010. It has been mesured by TIMED SEE and SORCE SOLSTICE calibrated to UARS SOLSTICE level [Woods et al., 2000] (provided by LASP, Laboratory For Atmospheric And Space Physics, University of Boulder, Colorado). With the function given by (Emerich et. al., 2005), the line-center solar Lyman-α flux was calculated from this total solar Lyman-α flux for the derivation of the g-factor as used in Equation (4).

The solar activity level as indicated by the solar $F_{10,7cm}$-radio flux starts to increase in summer 1999 from the low values of the solar minimum until 1998. With 130 the $F_{10,7cm}$-value during the UVIS/HDAC observations is also a bit higher compared to $\approx$ 80 during the TWINS LAD-observation in 2008 and 2010.

When flying at the Earth dayside between 3-15 R_e, the UVIS/HDAC LOS pointed to a region with

interplanetary Lyman-α background of about 1400 R. This value was taken from the SOHO-SWAN all sky map of the Lyman-α background of 17 August 1999 (SOHO-SWAN images provided via Web by LATMOS-IPSL, Universit Versailles St-Quentin, CNRS, France: http://swan.projet.latmos.ipsl.fr/images/).

4 Approach

During the swing by at the Earth, the UVIS/HDAC instrument measured Lyman-α radiation resonantly backscattered from neutral hydrogen of the terrestrial exosphere and also from the interplanetary medium. Due to their low velocities the contributing H-atoms can be considered as "cold". Therefore, this backscattered radiation contains wavelengths with a relatively narrow bandwidth around the Lyman-α line center. The sole contribution of the interplanetary hydrogen was quantified by the value taken from SOHO-SWAN as described in the previous section.

Within the exosphere the optical depth turns to be lower than 1 at geocentric distances $> 3\ R_e$, which allows for the assumption of single scattering. Under this assumption for a particular solar Lyman-α radiation (manifested in the g-factor) the exospheric H-density $N(S)$ along a line of sight S produces a Lyman-α scatter intensity I in [R]:

$$I = \frac{g}{10^6} \int_0^{S_{max}} n(S)\epsilon(S)I_p(\alpha(S))dS \tag{4}$$

with $n(S)$ is the local H-density, $\epsilon(S)$ the local correction term for geocoronal selfabsorption/re-emission and $I_p(\alpha(S))$ the local intensity correction for the angular dependence of the scattering.

Additionally to the solar radiation the dayside Lyman-α observations above $3R_{\mathrm{e}}$ analysed in this study are illuminated by a secondary Lyman-α radiation from lower atmospheric shells of the Earth: At the dayside lower, optically thick exospheric shells are face-on illuminated by the Sun. The re-emission created there acts as a secondary source of Lyman-α besides the Sun. The relative effect increases with decreasing geocentric distance. With the $\epsilon(S)$-term in Equation (4) the Lyman-α intensity profile can be corrected from re-emission of solar Lyman-α from lower atmospheric shells of the Earth. The applied method in this study, all considered correction terms and the used $\epsilon(r, \theta, \phi)$ map (shown in Figure 2) are in detail described in (Zoennchen et al., 2015).

With usage of a given H-density distribution the Lyman-α column brightness can be calculated for any LOS and observing position within the optically thin regime based on the integral in Equation (4). The calculated values ([R]) can be converted into their observable intensities ([counts/s]) using a single instrumental factor ([counts/s/R]) - further refered as conversion factor f_c.

In this study two H-density models are used for comparison with UVIS/HDAC: the exospheric $H(r, \theta, \phi)$-density model derived from TWINS Lyman-α observations from 2008 and 2010 (Zoennchen et al., 2015 - with parameters from Table 1 there) and a radial symmetric model as introduced by (Chamberlain, 1963) and frequently used for example by (Rairden et al., 1986), (Fuselier et al.,

2010, 2020) or (Connor & Carter, 2019):

$$n_H(r) = n_0 \cdot \left(\frac{10\ R_e}{r}\right)^3 \quad (5)$$

with the geocentric distance r in R_e. The H-density at 10 R_e subsolar point (n_0) is set at 40 cm^{-3}, which is within the reported range of Connor & Carter (2019) that derived n_0 from the XMM soft X-ray emission.

The used TWINS model is an empirical 3D model of the neutral exospheric H-density with validity range 3-8 R_e. It based on the inversion of Lyman-α LOS-observations of the TWINS satellites from the solar minimum in 2008 and 2010.

The other density model was introduced by [Chamberlain, 1963] as analytical approach, that based on 3 different H-atom populations in the exosphere (ballistic, satellite and escaping) with an initial Maxwellian distribution function at the exobase and the assumption of constant distribution functions on H-atoms trajectories (Liouville's theorem). The theoretical fundamentals are very good summarized in [Beth et al., 2016].

The comparison of the calculated profiles with the UVIS/HDAC profile was made for two reasons: First, to compare their radial dependency and second, to derive the conversion factor f_c of UVIS/HDAC by cross-calibrating it against the calculated profile from the TWINS H-density model in the radial range 3.0-5.5 R_e (overlapping range). Dayside Lyman-α observations with impact distances inside this overlapping range are available by both - UVIS/HDAC and TWINS. This method for evaluation of f_c assumes, that the TWINS H-density model from 2008, 2010 also matches the exospheric H-density distribution on 18 August 1999 due to comparable space weather conditions. Both, the used TWINS and UVIS/HDAC observations were measured during quiet geomagnetic conditions (minimum Dst index $\approx$ -30 nT; provided by the website of the WDC for Geomagnetism, Kyoto) and low solar activity (Solar 10,7 cm $\leq$ 130).

Nevertheless, it is known from other studies, that the terrestrial exosphere show H-density variations of about 10-20$\%$ caused by geomagnetic storms (i.e. Bailey & Gruntman, 2013; Zoennchen et al., 2017; Cucho-Padin & Waldrop, 2018). Therefore we expect an error of the conversion factor by this variations up to 20$\%$.

5 Comparison of the observed UVIS/HDAC profile with calculated profiles

The observed dayside Lyman-α profile (column intensity) by UVIS/HDAC (approximated in Equation (2)) was compared to the calculated Lyman-α profiles (column brightness) from two exospheric H-density models described in the previous section. CASSINI's trajectory at the dayside between 3-15 R_e, the LOS of HDAC, the interplanetary background and the solar conditions of the swing by day 18 August 1999 were considered by the calculation.

Figure (3A) shows the uncorrected observed Lyman-α profile by UVIS/HDAC from Equation (2) in [counts/s] (black line) together with the calculated column brightness profiles in [R] based on the

TWINS 3D H-density model (inside its validity range 3-8 R_e = red line) and the $1/R^3$ model (blue line) - all including interplanetary Lyman-α background. It is obvious from that figure, that between 3-8 R_e the radial dependence of the calculated profile using the TWINS 3D H-density model corresponds well to the UVIS/HDAC observed profile. The radial dependency of the $1/R^3$-profile (blue line) deviates from the HDAC profile in this particular range.

Figure (3B) shows the ratios of the observed and the calculated profiles: In the overlapping range (3.0-5.5 R_e) the averaged ratio between the UVIS/HDAC observations and the TWINS 3D H-density model (red line) is nearly constant with only slight variations between -2.1% and +1.2%. It is equivalent to the averaged conversion factor and was found to be f_c=3.285 [counts/s/R].

For the $1/R^3$ model (blue line) the ratio shows significant deviations from a constant value for lower radial distances $<8R_e$. But for distances above 9 R_e the profile of this model turned also into a nearly constant ratio to the UVIS/HDAC data (average = 3.145 [counts/s/R]).

Besides the cross-calibration method there is another independent way to approximate f_c: (Werner et al, 2004) estimated the interplanetary Lyman-α background in the UVIS/HDAC observations with 4500 [counts/s]. To be not contaminated with exospheric emission, this value had to be measured far enough outside the exosphere. The interplanetary Lyman-α radiation is also created by resonant backscattering and is therefore comparable in its physical properties to exospheric emission. Using the Lyman-α background emission value from SOHO-SWAN in [R] for the UVIS/HDAC LOS, the conversion factor f_c can be approximated on this separate way to:

$$f_c = \frac{4500\ counts/s}{1400\ R} = 3.215\ [counts/s/R] \tag{6}$$

The two results for f_c with f_c=3.285 from the profile comparison using the TWINS H-density model and f_c=3.215 from the background estimation by (Werner et al., 2004) are relatively close together.

6 H-density profile derived from the UVIS/HDAC observations

We applied the determined conversion factor f_c=3.285 [counts/s/R] to convert the observed dayside Lyman-α profile by UVIS/HDAC from intensities [counts/s] into column brightness [R] between 3-15 R_e. Inverse usage of Equation (4) with known column brightnesses I(S) allows to fit the H-density profile. The H-density profile inverted from the UVIS/HDAC observations was fitted into the radial symmetric function:

$$n_H(r) = 370520 * (r + 2.47)^{-3.67}\ \ [cm^{-3}] \tag{7}$$

with geocentric distance r in R_e. Figure (4) shows the fitted H-density profile (black squares). From the $n_H(r)$-profile the UVIS/HDAC observations can be calculated very precisely over the entire radial range 3-15 R_e within $\pm$ 2% error.

Obvious in Figure (4) is a change in the radial dependency of the profile in the radial region above

8 R_e. At distances lower 8 R_e the H-density profile seems to fall with distance with a power law $\approx r^{-2.37}$ (red line in Figure (4)). It was fitted in the distance range 3-7 R_e to:

$$n_H(r) = 10198 * r^{-2.375} \quad [cm^{-3}] \tag{8}$$

where the geocentric distance r is in R_e. The black and red lines are in very good agreement at 3-7 R_e. Above >8 R_e the situation has changed and the H-density falls with about $\approx r^{-3}$, what is indicated by the very good agreement of the cyan with the black squares there. The fit of the H-density profile between 9-15 R_e delivers a r^{-3} fall:

$$n_H(r) = 35.17 * \left(\frac{10\ R_e}{r}\right)^{3.02} \quad [cm^{-3}] \tag{9}$$

From theory an enhanced loss of neutral H atoms near the magnetopause and outside the magnetosphere can be expected due to sharply increased interactions with solar wind ions in this region that produces soft X-ray photons and ENAs. The faster decrease with r^{-3} in the H-density profile above 8 R_e might indicate the higher ionization of cold exospheric neutrals near the magnetopause (located at 9-11 R_e in the vicinity of the sub solar point) and beyond.

From the fitted H-density profile of Equation (7) the exospheric H-density at 10 R_e was found to be 35 cm^{-3} at the ecliptic dayside. From known variations of the neutral exosphere due to geomagnetic storms up to 20 % [Zoennchen et al., 2017] and with the summarized error from other contributions (i.e. from background, solar Lyman-α flux and so on) there is a total error in the H-density of about 25 % expectable. Nevertheless, from several facts we assume, that the found value of 35 cm^{-3} at 10 R_e is more likely to be a lower limit: First, between 3-10 R_e the neutral exospheric response to geomagnetic storms is so far known as an increase and not as a decrase of neutral density (Bailey & Gruntman 2013, Zoennchen et al., 2017, Cucho-Padin & Waldrop 2018). Second, there are indications, that an increasing solar activity also corresponds to an increase of neutral density in this radial range, either weak (Fuselier et al., 2020) or somewhat stronger (Zoennchen et al., 2015). The H-density model from TWINS used here based on observations in 2008 and 2010 near solar minimum during quiet days without storms. Therefore it represents likely an exosphere with neutral densities close to their lowest values.

7 Discussion

Ecliptic dayside Lyman-α observations of the terrestrial H-exosphere between 3-15 R_e by UVIS/HDAC onboard CASSINI were compared to calculated Lyman-α brightnesses using two different H-density models: First, the H-density model based on TWINS Lyman-α observations from 2008, 2010 and second, the $1/R^3$-model introduced by (Chamberlain et al., 1963). The calculations considered the HDAC Lyman-α observations, CASSINIs trajectory and the HDAC LOS published by (Werner et al., 2004).

As first result it was found, that the radial dependence of the HDAC observations and the calculated

profile from the TWINS model are very similar in the radial range 3-8 R_e. The $1/R^3$-model shows significant deviations from the observed profile in this lower range.

To be able to convert the HDAC observations from [counts/s] into physical units [R] the averaged conversion factor f_c=3.285 [counts/s/R] was derived in the radial range 3.0-5.5 R_e (overlapping region) from the ratio between the HDAC observations and the calculated Lyman-α brightnesses from the TWINS model. Dayside LOSs with impact distances in the overlapping region are available from both instruments - HDAC and TWINS LAD. Additionally a second independent way was used to quantifiy the conversion factor f_c=3.215 [counts/s/R] by calculating the ratio between the estimated background value given by (Werner et al., 2004) and the corresponding value taken from the SOHO/SWAN map. Both values found for f_c are very close together.

With usage of f_c=3.285 the HDAC observations are inverted into a radial symmetric H-density profile of the ecliptic dayside between 3-15 R_e. The derived density profile determined a H-density value of 35 cm^{-3} at 10 R_e in the vicinity of the sub-solar point. The error is expected with 25 $\%$. Nevertheless, from different mentioned reasons it is more likely, that this value is closer to the lower limit.

Also found was a faster decrease of the H-density for distances above 8 R_e (r^{-3}) compared to the lower region 3-7 R_e ($r^{-2.37}$). This is consistent with an enhanced depletion of neutral H in the far-upsun direction beyond 8 R_e reported by (Carruthers et al, 1976) based on Lyman-α images from the Moon by Apollo 16 and also with observations of Mariner 5 (Wallace et al., 1970).

The faster H-density decrease above 8 R_e in the up-sun direction as quantified in this study may indicate an enhanced ionization rate near the magnetopause and beyond, respectively, due to sharply increased interactions there of neutral H atoms with solar wind ions.

The regions near the sub solar point (close to the magnetopause) and the connected magnetosheath are identified as sources of observable strong enhanced ENA production (see e.g. Fuselier et al., 2010, 2020) and of Soft X-ray radiation (see Connor & Carter, 2019).

The ENA's are produced by charge exchange between energized solar wind H^+-ions and cold geocoronal neutral H. The result is a slow H^+-ion (bound to the terrestrial magnetic field) and a fast neutral H-atom (ENA), which mainly escapes from this region into space.

The Soft X-ray radiation is (also) produced by charge exchange - between highly charged solar wind oxygen ions (O^{7+} or O^{8+}) and geocoronal neutral H, which donates an electron to the ions (referred as solar wind charge process SWCX).

Inside the magnetopause there is a protection against the solar wind ions due to the terrestrial magnetic field. This situation changes from the magnetopause towards the connected magnetosheats: There, the named ENA- and Soft X-ray production sharply increase, since the solar wind ions can penetrate this regions.

In both processes cold neutral H-atoms are lost by conversion into ions. This might be a possible reason for a faster decrease of the neutral geocoronal H-density in the named regions of ENA / Soft

X-ray production.

Acknowledgements. The authors gratefully thank the TWINS team (PI Dave McComas) for making this work possible. Hyunju K. Connor gratefully acknowledges support from the NSF grants, AGS-1928883 and OIA-1920965, and the NASA grants, 80NSSC18K1042, 80NSSC18K1043, 80NSSC19K0844, 80NSSC20K1670, and 80MSFC20C0019. We acknowledge the support from the International Space Science Institute on the ISSI team 492, titled ”The Earth’s Exosphere and its Response to Space Weather”.

References

Bailey, J., & Gruntman, M. (2011). Experimental study of exospheric hydrogen atom distributions by Lyman-α detectors on the TWINSmission. Journal of Geophysical Research, 116, A09302. https://doi.org/10.1029/2011JA016531

Bailey, J., & Gruntman, M. (2013). Observations of exosphere variations during geomagnetic storms. Geophysical Research Letters, 40, 1907-1911. https://doi.org/10.1002/grl.50443

Baliukin, I., Bertaux, J.-L., Quemerais, E., Izmodenov, V., & Schmidt, W. (2019). SWAN/SOHO Lyman-α mapping: The hydrogen geocorona extends well beyond the Moon. Journal of Geophysical Research: Space Physics, 124, 861-885. https://doi.org/10.1029/2018JA026136

Beth A., Garnier P., Toublanc D., Dandouras I., Mazelle C.(2016). Theory for planetary exospheres: II. Radiation pressure effect on exospheric density profiles. Icarus, Volume 266, 2016, Pages 423-432, ISSN 0019-1035, https://doi.org/10.1016/j.icarus.2015.08.023.

Bishop, J., Geocoronal structure: The effect of solar radiation pressure and. plasmasphere interaction, J. Geophys. Res., 90, 5235- 5245, 1985.

Branduardi-Raymont, G., Wang, C., Dai, L., Donovan, E., Li, L., Sembay, S., et al. (2018). SMILE Definition study report (red book). ESA/SCI(2018)1. Retrieved from https://sci.esa.int/web/smile/-/61194-smile-definition-study-report-red-book

Carruthers, G. R., Page, T., and Meier, R. R. (1976): Apollo 16 Lyman alpha imagery of the hydrogen geocorona, J. Geophys. Res., 81, 1664-1672 https://doi.org/10.1029/JA081i010p01664

Chamberlain, J. W.: Planetary coronae and atmospheric evaporation, Planet Space Sci., 11, 901-960, 1963.

Connor, H. K. and Carter, J. A. (2019), Exospheric neutral hydrogen density at the 10 R_e subsolar point deduced from XMM-Newton X-ray observations, Journal of Geophysical Research: Space Physics, doi:10.1029/2018JA026187.

Connor, H. K., Sibeck, D. G., Collier, M. R., Baliukin, I. I., Branduardi-Raymont, G., Brandt, P. C., et al. (2021). Soft X-ray and ENA imaging of the Earth's dayside magnetosphere. Journal of Geophysical Research: Space Physics, 126, e2020JA028816. https://doi.org/10.1029/2020JA028816

Cucho-Padin, G., & Waldrop, L. (2019). Time-dependent Response of the Terrestrial Exosphere to a Geomagnetic Storm. Geophysical Research Letters, 46. https://doi.org/10.1029/2019GL084327

Domingo, V., Fleck, B., & Poland, A. I. (1995). SOHO: The solar and heliospheric observatory. Space Science Reviews, 72, 81. https://doi.org/10.1007/BF00768758

Emerich, C., Lemaire, P., Vial, J.-C., Curdt, W., Schühle, U., Wilhelm, K. (2005): A new relation between the central spectral solar HI Lyman-α irradiance and the line irradiance measured by SUMER/SOHO during the cycle 23, Icarus, 178, 429-433. https://doi.org/10.1016/j.icarus.2005.05.002

Fahr, H. J., Nass, U., Dutta-Roy R. & Zoennchen, J. H. (2018): Neutralized solar wind ahead of the Earth's magnetopause as contribution to non-thermal exospheric hydrogen. Ann. Geophys., 36(2), 445-457. https://doi.org/10.5194/angeo-36-445-2018

Fuselier, S. A., Funsten, H. O., Heirtzler, D., Janzen, P., Kucharek, H., McComas, D. J., et al. (2010). Energetic neutral atoms from the Earth's sub-solar magnetopause. Geophysical Research Letters, 37, L13101. https://doi.org/10.1029/2010GL044140

Fuselier, S. A., Dayeh, M. A., Galli, A., Funsten, H. O., Schwadron, N. A., Petrinec, S. M., et al. (2020). Neu-

tral atom imaging of the solar wind-magnetosphere-exosphere interaction near the subsolar magnetopause. Geophysical Research Letters, e2020GL089362. 47. https://doi.org/10.1029/2020GL089362

Goldstein, J., & McComas, D. J. (2018). The big picture: Imaging of the global geospace environment by the TWINS mission. Reviews of Geophysics, 56, 251-277. https://doi.org/10.1002/2017RG000583

Hodges Jr., R. R. (1994), Monte Carlo simulation of the terrestrial hydrogen exosphere, J. Geophys. Res., 99, 23229-23247.

Jansen, F., Lumb, D., Altieri, B., Clavel, J., Ehle, M., Erd, C., et al. (2001). XMM-Newton observatory: I. The spacecraft and operations. Astronomy and Astrophysics, 365(1), L1-L6. https://doi.org/10.1051/0004-6361:20000036

Kusnierkiewicz, D. Y., "A description of the TIMED spacecraft," American Institute of Physics (AIP) Conference Proceedings, 387, Part One, pp. 115-121, 1997

McComas, D. J., Allegrini, F., Bochsler, P., Bzowski, M., Christian, E. R., Crew, G. B., et al. (2009). Global observations of the interstellar interaction from the Interstellar Boundary Explorer (IBEX). Science, 326, 959-962. https://doi.org/10.1126/science.1180906

Qin, J., and L. Waldrop (2016), Non-thermal hydrogen atoms in the terrestrial upper thermosphere, Nat. Commun., 7, 13655, doi:10.1038/ncomms13655.

Qin, J., Waldrop, L., & Makela, J. J. (2017). Redistribution of H atoms in the upper atmosphere during geomagnetic storms. Journal of Geophysical Research: Space Physics, 122, 10686-10693. https://doi.org/10.1002/2017JA024489

Sibeck, D. G., Allen, R., Aryan, H., Bodewits, D., Brandt, P., Branduardi-Raymont, G., et al. (2018). Imaging plasma density structures in the soft X-rays generated by solar wind charge exchange with neutrals. Space Science Reviews, 214(4), 124. article id. 79.

Waldrop, L., and L. J. Paxton (2013), Lyman-α airglow emission: Implications for atomic hydrogen geocorona variability with solar cycle, J. Geophys. Res. Space Physics, 118, 5874-5890. https://doi.org/10.1002/jgra.50496

Wallace, L., Barth, C. A., Pearce, J. B., Kelly, K. K., Anderson, D. E., and Fastie, W. G. (1970): Mariner 5 measurement of the Earth's Lyman alpha emission, J. Geophys. Res., 75(19), 3769-3777. https://doi.org/10.1029/JA075i019p03769.

Werner S., Keller H.U., Korth A., Lauche H. (2004): UVIS/HDAC Lyman-α observations of the geocorona during Cassinis Earth swingby compared to model predictions, Advances in Space Research, Volume 34, Issue 8, 2004, Pages 1647-1649, ISSN 0273-1177. https://doi.org/10.1016/j.asr.2003.03.074

Woods, T. N., Tobiska, W. K., Rottman, G. J., and Worden, J. R. (2000): Improved solar Lyman alpha irradiance modeling from 1947 through 1999 based on UARS observations, J. Geophys. Res., 105, 27195-27215. https://doi.org/10.1029/2000JA000051

Zoennchen, J. H., Bailey, J. J., Nass, U., Gruntman, M., Fahr, H. J., & Goldstein, J. (2011). The TWINS exospheric neutral H-density distribution under solar minimum conditions. Annales de Geophysique, 29(12), 2211-2217. https://doi.org/10.5194/angeo-29-2211-2011

Zoennchen, J. H., Nass, U., and Fahr, H. J. (2013): Exospheric hydrogen density distributions for equinox and summer solstice observed with TWINS1/2 during solar minimum, Ann. Geophys., 31, 513-527. https://doi.org/10.5194/angeo-31-513-2013

Zoennchen, J. H., Nass, U., and Fahr, H. J. (2015): Terrestrial exospheric hydrogen density distributions under solar minimum and solar maximum conditions observed by the TWINS stereo mission, Ann. Geophys., 33, 413-426. https://doi.org/10.5194/angeo-33-413-2015

Zoennchen, J. H., Nass, U., Fahr, H. J., & Goldstein, J. (2017): The response of the H geocorona between 3 and 8 R_{e} to geomagnetic disturbances studied using TWINS stereo Lyman-α data. Ann. Geophys., 35(1), 171-179. https://doi.org/10.5194/angeo-35-171-2017

Figure Captions

Fig. 1. Black: UVIS/HDAC Lyman-α intensity profile [counts/s] (black line) from (Werner et al., 2004); the origin of the two peaks were identified by (Werner et al., 2004) as (A) the Earthmoon and (B) distortion by the radiation belt; Red: numerical approximation of the intensity profile from Equation (1).

Fig. 2. Local ratio $\epsilon(r, \theta, \phi)$ of the local Lyman-α illumination (influenced by multiple scattering effects) and the original solar illumination within the ecliptic plane calculated with a multiple scattering Monte Carlo model (Zoennchen et al., 2015).

Fig. 3. (A) observed, uncorrected Lyman-α profile by UVIS/HDAC in [counts/s] from Equation (2) (black line) and the calculated column brightness profiles based on the TWINS 3D H-density model (red line) and the $1/R^3$ model (blue line), both including background and in [R]
(B) ratios between the UVIS/HDAC observed and the calculated profiles: with the TWINS H-density model (red line) and with the $1/R^3$ model (blue line).

Fig. 4. (Black squares): Radial symmetric H-density profile (Equation (7)) fitted from UVIS/HDAC observations; (Red line): Powerlaw fit of the H-density profile in the lower radial range 3-7 R_{e}; (Cyan line): Powerlaw fit of the H-density profile in the upper radial range 9-15 R_{e}; The deviation of the red and the cyan lines from the black squares indicate, that the H-density profiles falls faster at larger distances >8 R_{e} than at lower distances <8 R_{e}.

Figures:

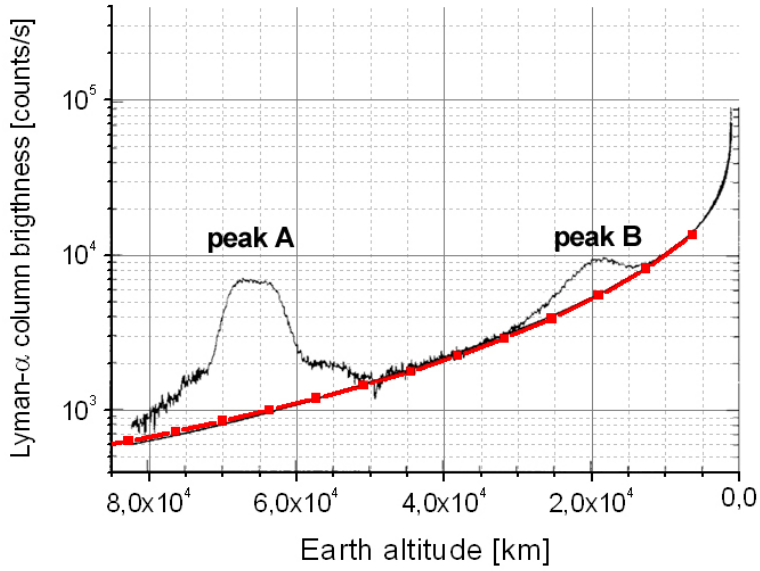

Fig. 1. Black: UVIS/HDAC Lyman-α intensity profile [counts/s] (black line) from (Werner et al., 2004); the origin of the two peaks were identified by (Werner et al., 2004) as (A) the Earthmoon and (B) distortion by the radiation belt; Red: numerical approximation of the intensity profile from Equation (1)

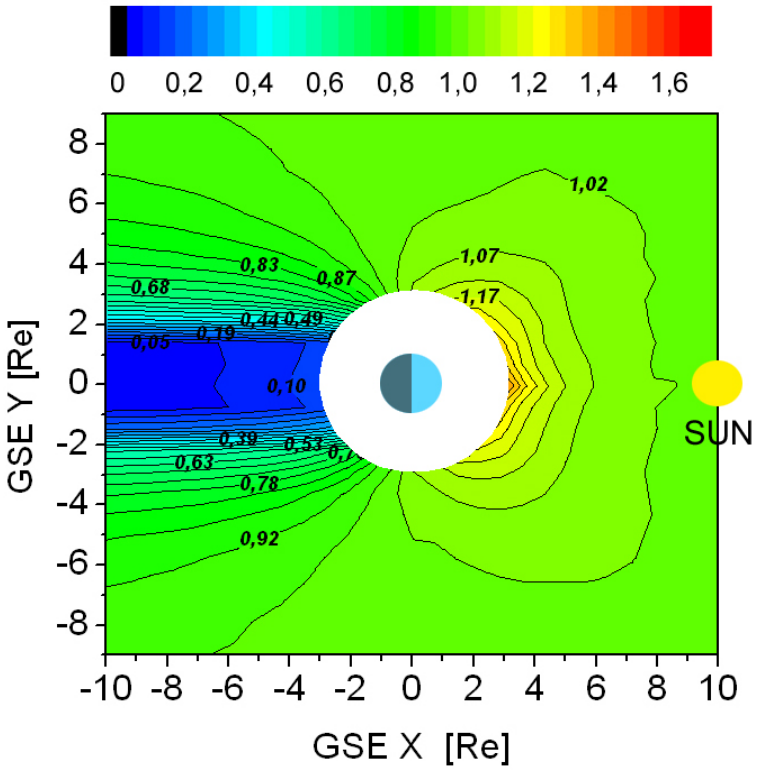

Fig. 2. Local ratio ε(r,θ,φ) of the local Lyman-α illumination (influenced by multiple scattering effects) and the original solar illumination within the ecliptic plane calculated with a multiple scattering Monte Carlo model (Zoennchen et al., 2015)

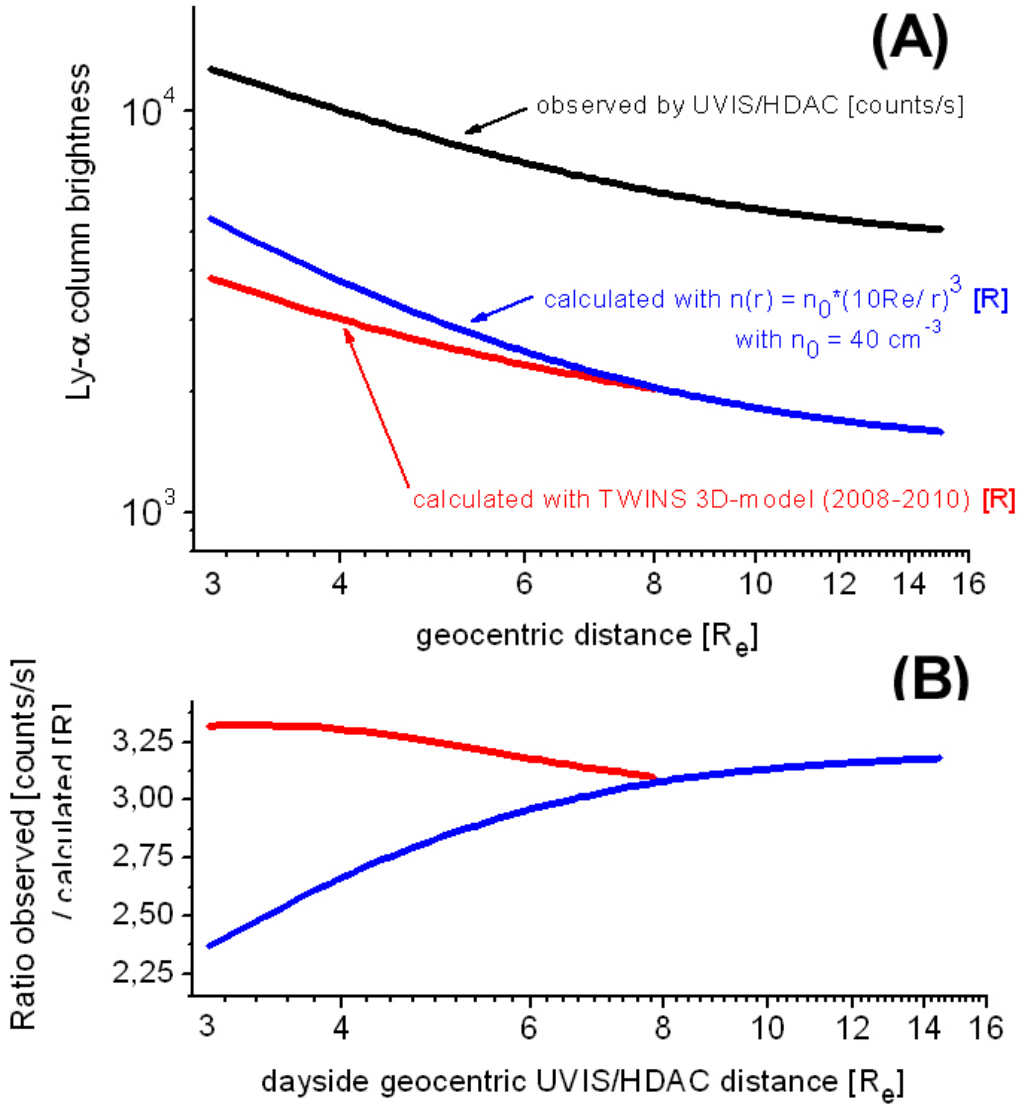

Fig. 3. (A) observed, uncorrected Lyman-α profile by UVIS/HDAC in [counts/s] from Equation (2) (black line) and the calculated column brightness profiles based on the TWINS 3D H-density model (red line) and the $1/R^3$ model (blue line), both including background and in [R]
(B) ratios between the UVIS/HDAC observed and the calculated profiles: with the TWINS H-density model (red line) and with the $1/R^3$ model (blue line).

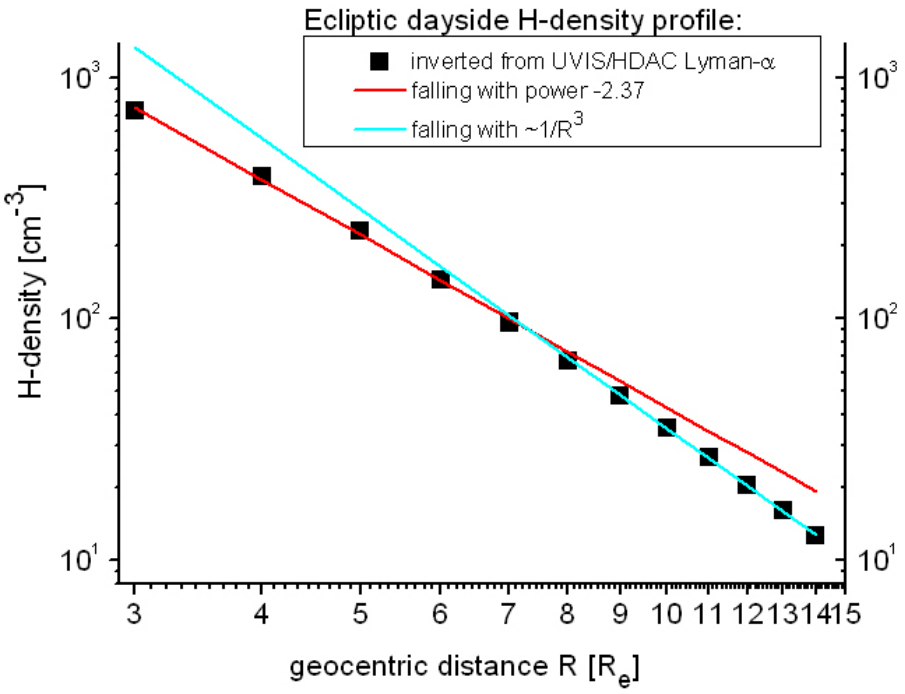

Fig. 4. (Black squares): Radial symmetric H-density profile (Equation (7) fitted from UVIS/HDAC observations; (Red line): Powerlaw fit of the H-density profile in the lower radial range 3-7 R_e; (Cyan line): Powerlaw fit of the H-density profile in the upper radial range 9-15 R_e; The deviation of the red and the cyan lines from the black squares indicate, that the H-density profiles falls faster at larger distances >8 R_e than at lower distances <8 R_e.